An SMA Survey of HNC Chemistry in Transition Disks

Kyle Gresko
Charles Law, L. Ilsedore Cleeves, Deryl Long

Department of Astronomy
University of Virginia

This thesis is submitted in partial completion of
the requirements of the B.S. Astronomy-Physics Major.

May 9, 2025

ABSTRACT

Planets are directly influenced by the chemical environments of the protoplanetary disks (PPDs) in which they form. Hydrogen cyanide (HCN) is a commonly-detected molecule in PPDs and has been widely used as a tracer of disk properties. However, its isomer, HNC, has rarely been targeted in PPDs, despite its frequent use in a variety of other astrophysical settings. Here, we present new Submillimeter Array observations of five transition disks, which include both the J=3–2 and J=4–3 lines of HCN and HNC. We detect at least one transition of HNC in four disks, more than doubling the total number of PPDs with HNC detections. From these observations, we measured disk-integrated fluxes, which we used to determine the rotational temperatures and column densities for each molecule. We then explored the HNC/HCN column density ratio and how it relates to UV radiation and disk temperature. We compared measured HNC line intensities to previous modeling by Long et al. (2021) and found that our measured fluxes are significantly higher, indicating that an unexpectedly active HNC chemistry may be occurring in transition disks. Although tentative due to the small sample size, these trends provide strong motivation for the continued investigation of HNC beyond our pilot study.

1. INTRODUCTION

1.1. *The Basics of Disk Chemistry and Structure*

Protoplanetary disks form as molecular clouds gravitationally collapse (Williams & Cieza 2011). The young protostars are surrounded by remaining dust and gas from the molecular cloud phase. These disks are capable of forming terrestrial and gaseous planets from their constituent dust and gas (Öberg et al. 2023). They are active and changing objects, with evolution driven by physical and chemical processes. Here, we are specifically concerned with Class II disks, which are thought to be the sites of active planet formation. Earlier stages in young stellar object evolution include a large surrounding cloud of gas and dust. However, by the Class II stage, the molecular cloud has condensed into a relatively flat, rotating disk. As detailed by Öberg et al. (2023), the dynamic processes in these objects are largely driven by stellar radiation, including both X-Ray and UV radiation. Furthermore, cosmic rays, produced by the system and beyond the system, interact with the disk's constituent gas and dust. That cold emission is especially observable by radio astronomy, in the range of submillimeter and millimeter wavelengths (Condon & Ransom 2016).

The vast majority of mass in a protoplanetary disk is tied up in gas, and the vast majority of the gas mass in a disk is tied up in H_2 (Öberg et al. 2023). Unfortunately, H_2 is not directly observable [except in the far-infrared (Williams & Cieza 2011)]. Furthermore, measuring physical characteristics like disk mass, accretion, and temperature profile of a protoplanetary disk can be difficult. Measurements typically include an intentional overestimation of the gas-to-dust ratio and an underestimation of the mass of large bodies.

To work around these troubles, well-understood molecular emission is often used as a proxy of disk characteristics. The CO molecule is used as a tracer of the presence of gas, but with the caveat that CO will freeze-out onto dust grains in outer disk regions with cold gas temperatures of ≤20K (Öberg et al. 2023). Isotopologues of CO (like ^{13}CO and ^{18}CO) are used to trace the snow lines of ^{12}CO when it is too optically thick to measure confidently. However, many properties cannot be measured using these molecules, and the search for further tracers continues.

1.2. *Transition Disks*

One crucial structural occurrence in protoplanetary disks is that of a transition disk. According to Van Der Marel (2023), full disks are the standard picture of the planetary birthplace. In the common full disk, the star is surrounded even at small radii by a dusty, gas-rich accretion disk. However, in a transition disk, a cavity lacking dust can be spatially resolved around the stellar object, even at smaller radii. Although the term was developed to imply the transition disk as a phase in the life cycle of a protoplanetary disk between full disk and a fully cleared-out disk, with only planets remaining, this idea is not necessarily true in all disks. With ALMA's prolific observations and high spatial resolution, many irregular disks have been observed. Regardless, the presence of a cavity affects the distribution of energy and material throughout a disk, which is observable in its SED (Van Der Marel 2023). In cases where giant planets are responsible for the presence of the clearing, by gravitational accretion into a planetesimal, more massive planets lead to sharper cavity "cliffs" as reported by Dong et al. (2017). Some small accretion disk may still remain around the star interior to the giant planet's orbit in this case. Photoevaporation by X-rays has also been suggested as an alternative mechanism to develop a cavity by Owen et al. (2017), although they note that this would only account for cavities out to ∼20 au and many transition disks have cavities out to 70 au or further (Dong et al. 2017). Although the dust has been cleared, gas can still be present within this cavity (Van Der Marel 2023). Measurements of accretion, like those made by Manara et al. (2014), indicate that material is being transported despite the apparent lack of material to transport. In general, a "gas cavity" tends to be more similar to the gas distribution of a full disk—a dust cavity demonstrates more drastic alteration (Van Der Marel 2023). Transition disks are also known to have asymmetries and a variety of substructures, indicating that multiple mechanisms may be affecting the resulting profiles (Manara et al. 2014).

1.3. *HNC Chemistry*

In non-protoplanetary disk contexts, hydrogen cyanide (HCN) and hydrogen isocyanide (HNC) are used as tracers of the gas temperature profile. The premise of the HNC/HCN tracer is that, in cold regions, the ratio should approach unity (Loison et al. 2014). This property has been used in planetary nebulae settings, interstellar medium settings, and, as demonstrated by Behrens et al. (2022), galactic settings. They used the brightness of HCN and HNC in all types of galaxies to study its distribution across the galaxy NGC 253.

It is suggested then that HNC and HCN might be used as a thermometer in disks as well by Long et al. (2021). HCN is well-observed and fairly bright in protoplanetary disks (Öberg et al. 2023) but HNC has only been detected previously in three disks. Graninger et al. (2015) observes the full disks around the T Tauri star TW Hya and Herbig Ae star HD 163296. Additionally Phuong et al. (2021) report detecting HNC in the T Tauri multistar system GG Tauri A. These detections were

Table 1. HNC Destruction Pathways

Reaction	Activation Temperature	Reaction
HNC + C → HCN + C	Constant w.r.t. T	(1)
HNC + O → CO + NH	T > 20 K	(2)
HNC + H → HCN + H	T > 200 K	(3)

NOTE—Destruction pathways for HNC in protoplanetary disks according to Loison et al. (2014).

obtained with the Submillimeter Array in Hawai'i and from the Northern Extended Millimeter Array in France. GG Tauri A, notably, is a transition disk.

Critical to the use of the HNC/HCN ratio are the formation and destruction pathways of each molecule. They involve similar formation pathways starting from nitrogen-based molecules as described by Loison et al. (2014):

$$\mathrm{HCNH^+ + e^- \rightarrow HCN + H}$$
$$\mathrm{HCNH^+ + e^- \rightarrow HNC + H}$$

It should be recognized that other formation pathways exist, including many that, at early timescales in the system, favor the production of HCN over HNC through the necessity that H^- bond to a carbon atom instead of a nitrogen. One critical example reaction is $H^- + CN \rightarrow HCN + e^-$ due to the H^-'s necessary binding to the carbon atom. The molecular abundances according to the predictions of Loison et al. (2014) are only fairly even (HNC/HCN$\approx$ 1) in situations of low carbon abundance.

In protoplanetary disks, Long et al. (2021) find that the HNC destruction pathways are the determining factor in the HNC/HCN ratio, because of the primary reactions described above. The destruction pathways can be seen in Table 1. Reaction (1) is constant with respect to temperature and thus cannot influence HNC/HCN as a tracer of temperature; reaction (2) needs an activation temperature of 20 K, and disks (especially the inner disk) tend to be at that temperature range. Therefore the crucial reaction is reaction (3) (Long et al. 2021).

Models have been used to describe the possible viability of HNC and HCN within full protoplanetary disks. Specifically, Long et al. (2021) used the Dust And Lines (DALI) chemical code to predict the emission of HCN and HNC, test its use as a thermometer (as in galactic contexts), and map its distribution compared to physical characteristics. The model incorporates chemistry of CNO from Visser et al. (2018) which includes the relevant HCN and HNC pathways. In terms of physical characteristics, disk mass, accretion rate, disk flaring, and dust distribution are considered for the HNC and HCN J=1–0 and J=3–2 emission lines in both T Tauri and Herbig stars. Additional models are considered for oxygen- and carbon-depleted circumstances. Predicted emission for both molecules tends to be higher in the Herbig stars due to their higher UV radiation rates—this is attributed to the radiation's affect on the formation pathway of HCN and HNC, where ionized $HCNH^+$ is necessary. The J=3–2 emission peaks signficantly closer to the stars (around 50-100 au) vs. the J=1–0 emission, which peaks around ∼300 au. In total, Long et al. (2021) evaluates the HNC/HCN ratio to not necessarily only trace temperature due to many convoluting results from

Table 2. Stellar and Disk Properties

Source	Dist.	SpT	M_*	L_*	Age	v_{sys}	incl.	P.A.	$r_{mm,cavity}$	$R_{mm,edge}$
	(pc)		($M_\odot$)	($L_\odot$)	(Myr)	(km s^{-1})	(°)	(°)	(au)	(au)
GM Aur	159[1]	K6[2]	1.1[3]	1.2[4]	∼2.5[5]	5.6[3]	53.2[6]	57.2[6]	40[6]	170[6]
J1604-2130	145[1]	K2[7]	1.2[8]	0.6[9]	∼5-10[10]	4.6[8]	6.0[10]	258.8[8]	83[8]	265[8]
LkCa 15	157[1]	K5[11]	1.2[12]	1.1[11]	∼5[11]	6.3[12]	50.2[13]	61.9[13]	76[13]	153[13]
GG Tau	150[1]	M0+M2, M3[14]	1.2[14]	0.67[15]	∼3[14]	6.5[16]	35.0[17]	7.0[17]	224[18]	260[18]
V4046 Sgr	73[1]	K5+K7[19]	1.8[20]	0.86[21]	∼12-23[22]	2.9[21]	34.7[21]	75.7[21]	31[23]	100[23]

Note—References are: 1. Gaia Collaboration et al. (2023); 2. Espaillat et al. (2010); 3. Teague et al. (2021); 4. Macías et al. (2018); 5. Kraus & Hillenbrand (2009); 6. Huang et al. (2020); 7. Preibisch & Feigelson (2005); 8. Stadler et al. (2023); 9. Carpenter et al. (2014); 10. Dong et al. (2017); 11. Donati et al. (2019); 12. Law et al. (2023); 13. Facchini et al. (2020); 14. Keppler et al. (2020); 15. Hartigan & Kenyon (2003); 16. Guilloteau et al. (1999); 17. Phuong et al. (2021); 18. Phuong et al. (2020); 19. Quast et al. (2000); 20. Flaherty et al. (2020); 21. Rosenfeld et al. (2012); 22. Mamajek & Bell (2014); 23. Martinez-Brunner et al. (2022). For GG Tau and V4046 Sgr, the stellar mass and luminosity are the sum of all of stars in each system.

other physical characteristics. They predict abundance ratios of HNC/HCN$\leq$0.2 across the disk, except for regions affected by oxygen and carbon abundances. Additionally, the ratio of concern here is sensitive to UV flux.

It is important to note that these models assume a full disk. In transition disks, increased UV flux permeating further into the outer disk could encourage the formation of HNC and HCN. That increased UV flux could also increase the temperature throughout the disk, activating the destruction pathway of reaction (3) and decreasing the overall flux from HNC. The models from Long et al. (2021) predict that increased accretion rates correspond to increased HNC, and it is unclear if this will hold in transition disks, where accretion processes are modified by the inner-disk cavity.

1.4. *Sample*

Our sample comprises five T Tauri stars and their protoplanetary disks, each with previous observations of HCN. They are GM Aur, GG Tau, J1604-2130, LkCa 15, and V4046 Sgr. These disks are known to have bright and extended emission from at least one of the HCN J=1–0, J=3–2, or J=4–3 lines. Each source is additionally a transition disk with a range of millimeter-dust cavities from as small as 25 au (V4046 Sgr) to as large as 225 au (GG Tau). This consistent stellar archetype with varying physical system parameters allows us to consider the extent of UV radiation, through cavity size, as well as related attributes like accretion rate, with a consistent underlying stellar environment. Details about each source are listed in Table 2.

Table 3. Molecular Line Properties

Species	Line	Frequency	E_u (K)	A_{ul} ($\log_{10}$ s^{-1})	g_u
HCN	J=3–2	265.886434	25.5	−3.0766	21
HCN	J=4–3	354.505478	42.5	−2.6860	27
HNC	J=3–2	271.981142	26.1	−3.0298	7
HNC	J=4–3	362.630303	43.5	−2.6392	9

NOTE—The spectroscopic constants for all lines are taken from the CDMS database (Müller et al. 2001, 2005; Endres et al. 2016).

In this thesis, we explore HNC chemistry in protoplanetary transition disks through measuring disk-integrated fluxes, column densities, optical depths, and rotational temperatures of molecular emission. We preliminarily evaluate HNC and HCN as tracers of UV radiation, temperature, and other physical attributes important for setting the properties of nascent planets.

2. OBSERVATIONS

2.1. *Observational Details*

The data utilized herein are observations of the GM Aur, GG Tau, LkCa 15, V4046 Sgr, and J1604-2130 disks between 26 June 2023 and 12 Nov 2023 with the Submillimeter Array (SMA)[1] as part of project 2023A-S019 (PI: C. Law). All sources were observed in the compact (COM) configuration, while GM Aur, GG Tau, and LkCa 15 also had data taken in the extended (EXT) configuration, which has baselines up to ≈220 m. Each observation used either 6 or 7 antennas with a $\tau_{225\mathrm{GHz}}$ between 0.03-0.12 mm. Table 4 provides a summary of the observations.

Each observation used the RX240 and RX345 receivers of the upgraded SWARM correlator, which provided 48 GHz of bandwidth. The lower frequency receiver covered 244.3-256.6 GHz and 264.3-276.6 GHz, while the higher frequency receiver included 333.8-346.1 GHz and 353.8-366.1 GHz. The tuning selection was motivated by the desire to simultaneously cover the J=3–2 and J=4–3 lines of both HCN and HNC.

We converted the raw data to CASA measurement sets using the `pyuvdata` (Hazelton et al. 2017) SMA reduction pipeline[2] in CASA version `v6.3`. To reduce data volume, we channel-binned by a factor of four for initial calibration. Depending on the source and configuration, we used 3c84, 3c454.3, or 3c279 for our passband calibrators, while Titan, Callisto, Ceres, or Uranus served as flux calibrators. Two of the following quasars (0510+180, 3c111, 1507-168, 1517-243, 1700-261, nrao53) were used as gain calibrators for each source. Table 4 lists all calibrators used.

[1] The Submillimeter Array is a joint project between the Smithsonian Astrophysical Observatory and the Academia Sinica Institute of Astronomy and Astrophysics and is funded by the Smithsonian Institution and the Academia Sinica.
[2] https://github.com/Smithsonian/sma-data-reduction

Table 4. Observational Details

Source	UT Date	Num. Ant.[a]	SMA config.	τ (225 GHz)	Calibrators Flux	Passband	Gain
GM Aur	2023 Nov 05	6	COM	0.04	Titan	3c84	0510+180, 3c111
	2023 Oct 22	7	EXT	0.07	Callisto	3c84	0510+180, 3c111
GG Tau	2023 Nov 12	7	COM	0.11	Uranus	3c84	0510+180, 3c120
	2023 Oct 30	7	EXT	0.09	Titan	3c84	0510+180, 3c120
J1604-2130	2023 Jun 26	7	COM	0.05	Ceres	3c454.3	1507-168, 1517-243
LkCa 15	2023 Nov 06	6	COM	0.03	Titan	3c84	0510+180, 3c111
	2023 Oct 20	7	EXT	0.12	Titan	3c84	0510+180, 3c111
V4046 Sgr	2023 Jul 14	7	COM	0.06	Callisto	3c279	1700-261, nrao530

[a]Number of antennas remaining after flagging.

2.2. *Imaging*

We first subtracted the continuum by manually identifying line-free channels using the `uvcontsub` task in CASA with a first-order polynomial. We then imaged all lines using the `tclean` task with Briggs weighting (`robust` = 2.0) and Keplerian masks generated with the `keplerian_mask` (Teague 2020) code. Keplerian mask parameters for each disk were based on the known stellar properties and disk geometry from the literature (Table 2). Images were binned in velocity to 1 km s^{-1}, and in a few cases 2 km s^{-1}, to maximize SNR. All images were `CLEAN`ed down to a 3σ level, where σ was the RMS noise, measured across five line-free channels of the dirty image. Table 5 summarizes all image properties. The typical beam size was $\approx$1″-3″, while the RMS noise ranged from $\approx$40-250 mJy beam^{-1} in channels with width 1km s^{-1} and from $\approx$75-360 mJy beam^{-1} in channels with width 2km s^{-1}.

3. RESULTS

3.1. *Line Detections and Integrated Fluxes*

We consider an individual molecular emission line to be 'detected' if its disk-integrated flux exceeds 3σ. We also require a peak 3σ intensity in at least two channels. These guidelines are line with previous studies, e.g., Bergner et al. (2019).

We do not spatially resolve either HCN or HNC line emission in our observations of J1604 or V4046 Sgr. For GM Aur, GG Tau, and LkCa 15, we marginally resolve the HCN J=3–2 lines. This includes not resolving any disk's millimeter-dust cavities. Because of this, we assume that most emission is coming from the cold, outer disk, which is best-observed by the SMA. Because of the lack of spatial resolution, we forgo kinematic analysis and instead focus our investigation on integrated fluxes.

We extracted line spectra for all disks via the `gofish` Python package (Teague 2019) with circular masks, including the hyper-fine lines, based on the extent of the emission in channel maps. We then used these spectra to compute the disk-integrated fluxes. We bootstrapped to estimate the uncertainties of the flux measurements by randomly-generating 100 circular masks at the disk positions and

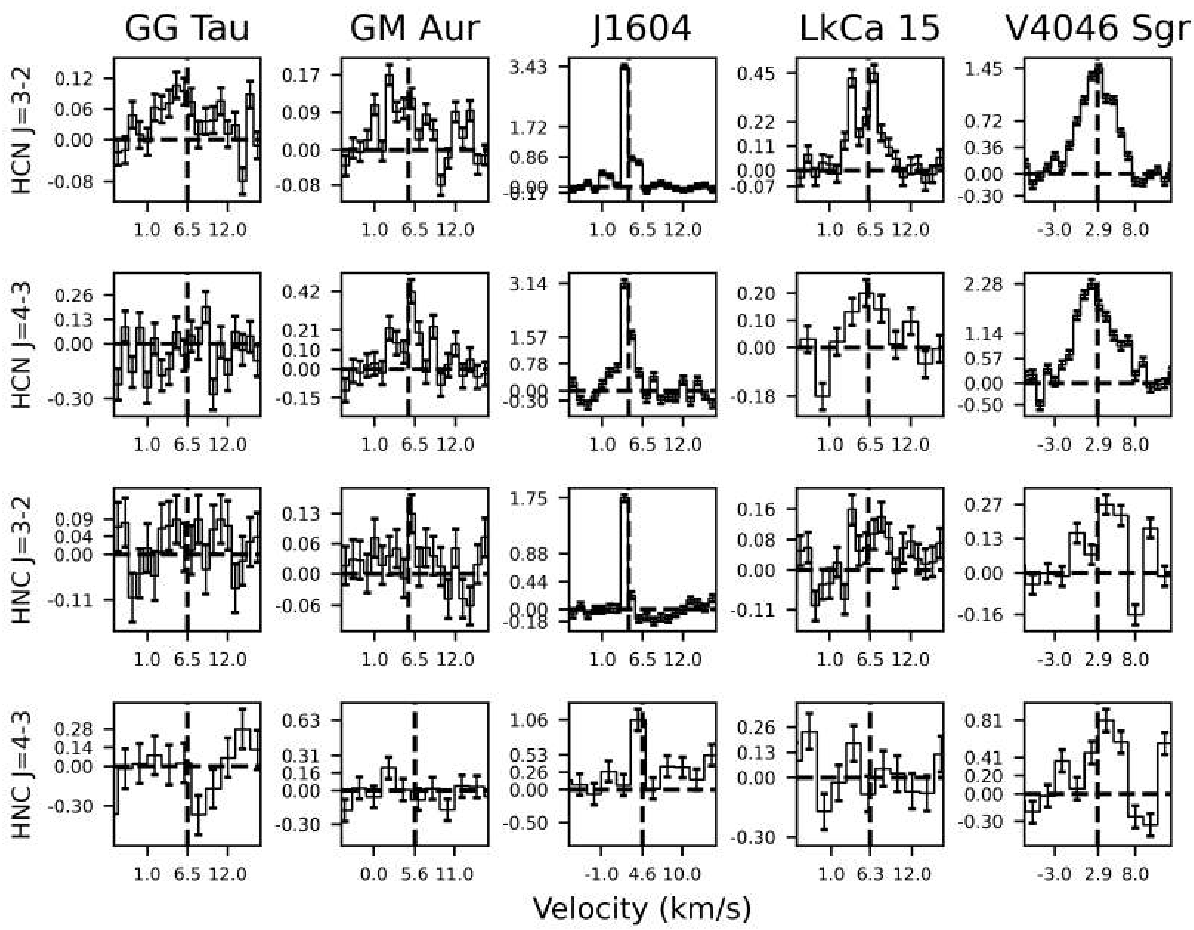

Figure 1. Gallery of spectra of the J=3–2 and J=4–3 lines of HCN and HNC in our SMA disk sample. All spectra were extracted in a circular aperture centered on the disk position. The dashed lines show the systemic velocity of each disk.

sizes but spanning only line-free channels, as done in Bergner et al. (2019). We take the uncertainty as the standard deviation of the integrated fluxes within these bootstrapped masks, as measured with tools from the `gofish` package (Teague 2019), added in quadrature with 10% of the measured flux to account for additional systemic flux calibration uncertainties.

We also incorporate the HCN hyper-fine lines in the total flux measurements. However, we note that many hyper-fine components are heavily blended with the main line component due to their close proximity in frequency-space and the relatively coarse spectral resolution of our imagecubes. These lines are all significantly weaker than the main line, as indicated by their Einstein coefficients. We sum flux from these lines into the image of the main line before integrating across the disk.

We have detected, in all disks, the HCN J=3–2 line. In all disks excluding GG Tau, we detect the HCN J=4–3 and HNC J=3–2. In only V4046 Sgr, we additionally detect HNC J=4–3 (the first detection of this line in a protoplanetary disk). Table 5 lists all flux measurements. Our non-detection of the HNC J=3–2 and J=4–3 lines in GG Tau is of note, as one of the three previous observations

Table 5. Image Cube Properties and Integrated Flux Measurements

Source	Line	Beam	Mask Radius	δv	RMS	Int. Flux
		($'' \times ''$, deg)	($''$)	(km s^{-1})	(Jy beam^{-1})	(Jy km s^{-1})
GM Aur	HCN J=3–2	2.25 × 1.30, 88.4	4.0	1.0	0.043	1.688 ± 0.261
	HCN J=4–3	1.81 × 1.04, 45.6	4.0	1.0	0.087	2.325 ± 0.461
	HNC J=3–2	2.21 × 1.27, 46.0	4.0	1.0	0.054	1.548 ± 0.379
	HNC J=4–3	1.71 × 0.98, 47.6	4.0	2.0	0.135	< 3.039
J1604-2130	HCN J=3-2	3.45 × 2.38, 7.9	4.0	1.0	0.113	6.576 ± 0.708
	HCN J=4-3	2.69 × 1.85, 11.7	4.0	1.0	0.268	10.619 ± 1.367
	HNC J=3-2	3.37 × 2.33, 8.0	4.0	1.0	0.131	2.612 ± 0.503
	HNC J=4-3	2.68 × 1.78, 13.3	4.0	2.0	0.360	< 5.090
LkCa 15	HCN J=3-2	2.29 × 1.31, 47.7	5.0	1.0	0.048	6.239 ± 0.652
	HCN J=4-3	1.87 × 1.09, 47.4	5.0	2.0	0.093	4.338 ± 0.731
	HNC J=3-2	2.23 × 1.28, 48.1	5.0	1.0	0.054	1.801 ± 0.344
	HNC J=4-3	1.75 × 0.99, 48.4	5.0	2.0	0.124	< 4.142
GG Tau	HCN J=3-2	1.69 × 1.25, 4.6	5.0	1.0	0.050	3.077 ± 0.480
	HCN J=4-3	1.21 × 0.94, 64.9	5.0	1.0	0.120	< 3.656
	HNC J=3-2	1.66 × 1.19, 74.9	5.0	1.0	0.081	< 1.766
	HNC J=4-3	1.12 × 0.79, 67.6	5.0	2.0	0.185	< 13.390
V4046 Sgr	HCN J=3-2	3.95 × 2.34, 9.2	4.0	1.0	0.098	13.926 ± 1.459
	HCN J=4-3	2.95 × 1.86, 6.5	4.0	1.0	0.254	19.532 ± 2.377
	HNC J=3-2	3.86 × 2.31, 9.5	4.0	2.0	0.075	2.096 ± 0.674
	HNC J=4-3	2.91 × 1.81, 4.7	4.0	2.0	0.297	14.988 ± 2.991

NOTE—For non-detections, we report 3σ upper limits.

of HNC in a protoplanetary disk was of the GG Tau HNC J=1–0 line by Phuong et al. (2021). This indicates that GG Tau is a colder disk, and does not activate the higher-J lines as readily.

3.2. *Rotational Temperatures, Column Densities, and Line Optical Depths*

To determine the gas excitation conditions in our disks, we adopted a rotational diagram approach Goldsmith & Langer (1999). To do so, we closely followed the approach outlined in Loomis et al. (2018). In short, from the measured fluxes and the upper state energies E_u we fit the data for N_u and T_{rot}, the column densities and rotational temperatures. We use the equation

$$I_\nu = \frac{A_{ul} N_u^{thin} hc}{4\pi \Delta v} \tag{1}$$

in which A_{ul} is the Einstein coefficient and Δv is the width of the line, for a molecule transitioning from rotational state u to rotational state l. As described in Section 3.1, we have derived our intensities $I_\nu = S_\nu/\Omega$, flux density / solid angle. Here we take Ω = the total area of our masked emission region. Our goal is to calculate N_u^{thin}, the column density of the molecule in that particular upper state u; to do this we also need to incorporate the equation

$$N_T = \frac{N_u Q_T}{g_u} e^{E_u/kT_{rot}} \tag{2}$$

which will allow us to leverage the upper state energy, E_u, and the rotational temperature of the molecule, T_{rot} (and by extension, the partition function Q which is a function of T_{rot}) to calculate the total column density of a molecule from a column density of a particular state u. However, rotational temperature T_{rot} and optical depth τ both are not directly observable quantities. We approximate optical depth as

$$\tau_{ul} = \frac{A_{ul} c^3 N_u}{8\pi\nu^3} (e^{(h\nu/kT_{rot})} - 1) \tag{3}$$

which once again relies on knowledge of N_u. Therefore, for HCN emission, we apply the Markov chain Monte Carlo code `emcee` (Foreman-Mackey et al. 2013) to calculate posterior probability distributions for T_{rot} and N_u, which we can then use to estimate τ. We take the best fit according to a linear least squares regression. We constrain the fit with priors of $10^{10} < N_T < 10^{14}$ cm^{-2} and $5 < T_{rot} < 80$ K, expect for V4046 Sgr where we constrain $10^{10} < N_T < 10^{14}$ cm^{-2} and $10 < T_{rot} < 100$ K due to the hotter nature of the disk.

We apply a correction $N_u = C_\tau N_u^{thin}$, where

$$C_\tau = \frac{\tau}{1 - e^{-\tau}}. \tag{4}$$

In the case of HNC for each disk except V4046 Sgr, our single line detection prevents us from utilizing a two-variable fit. Since all emission detected by the SMA is likely primarily from the outer disk regions, due to the large beam size, we assume the measured flux is coming from the same spatial regions for each molecule.

Although we had initially intended to incorporate the data from the GG Tau HCN and HNC J=1–0 transitions from Phuong et al. (2021), nondetections of any HNC line made this unnecessary. Although we consider our measurements for GG Tau, we adopt results from Phuong et al. (2021)- that is, from the colder J=1–0 emission line, an HCN column density of $N_T^{HCN} = (4.89 \pm 0.03) \times 10^{12}$ cm^{-2} and an HNC column density of $N_T^{HNC} = (2.47 \pm 0.02) \times 10^{12}$ cm^{-2}, for n(HNC)/n(HCN) ≈ 0.5. We find all molecules to be optically thin and temperatures to span the range of 11 K to 65 K, with

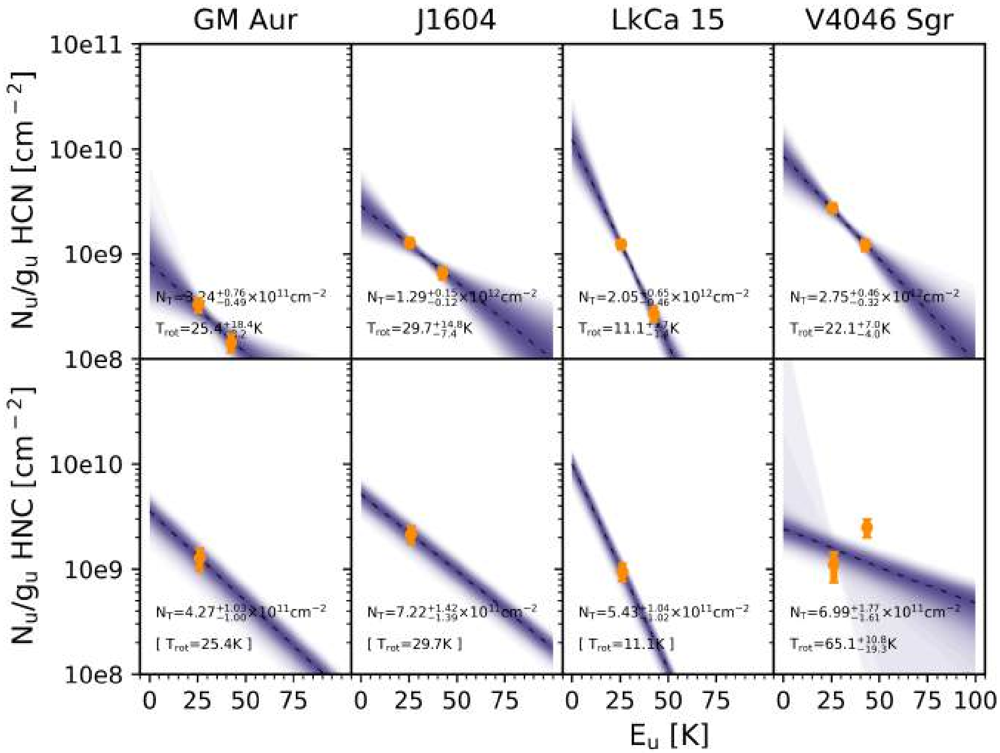

Figure 2. Gallery of rotational diagrams for HCN (*top row*) and HNC (*bottom row*) in our SMA disk sample. Purple shaded regions show random draws from the fit posteriors. We included a 10% calibration uncertainty on all measured fluxes.

a median of 25 K. HNC column densities are on the order of 10^{11} cm^{-2}, a factor of 10 less than the typical HCN values. Compared to the HCN column densities in Bergner et al. (2019), our J1604 HCN column density is within their uncertainty at 30K and our LkCa 15 HCN column density is within our uncertainty at 10K. (It should be noted that they assume an optically thick HCN as $\tau = 2$ or apply no correction; all of our HCN lines are estimated to be optically thin, which is reasonable in the less-dense outer disk.)

Table 6. Rotational Diagram Results

Source	Molecule	N_T (cm^{-2})	T_{rot} (K)	τ J=3–2	τ J=4–3
GM Aur	HCN	$3.27^{+0.75}_{-0.49}\times10^{12}$	$25.6^{+23.1}_{-8.1}$	6.14×10^{-3}	7.28×10^{-3}
	HNC	$4.32^{+1.05}_{-1.05}\times10^{11}$	[25.6]	2.99×10^{-3}	
J1604	HCN	$1.30^{+0.15}_{-0.12}\times10^{12}$	$29.5^{+15.3}_{-7.3}$	4.30×10^{-3}	3.99×10^{-3}
	HNC	$7.21^{+1.42}_{-1.38}\times10^{11}$	[29.5]	9.42×10^{-3}	1.19×10^{-3}
LkCa 15	HCN	$1.92^{+0.39}_{-0.38}\times10^{12}$	$11.5^{+1.5}_{-1.0}$	2.35×10^{-3}	2.17×10^{-3}
	HNC	$5.18^{+0.97}_{-1.01}\times10^{11}$	[11.5]	1.30×10^{-2}	
V4046 Sgr	HCN	$2.76^{+0.46}_{-0.34}\times10^{12}$	$22.2^{+6.6}_{-4.1}$	5.89×10^{-2}	6.29×10^{-2}
	HNC	$8.01^{+2.02}_{-1.93}\times10^{11}$	$80.5^{+14.2}_{-22.5}$	4.15×10^{-2}	2.01×10^{-2}

NOTE—GM Aur, J1604, and LkCa 15 were calculated using by adopting the rotational temperature from their respective HCN rotational diagrams, as indicated by brackets. Throughout this thesis, GG Tau's column densities are obtained from Phuong et al. (2021).

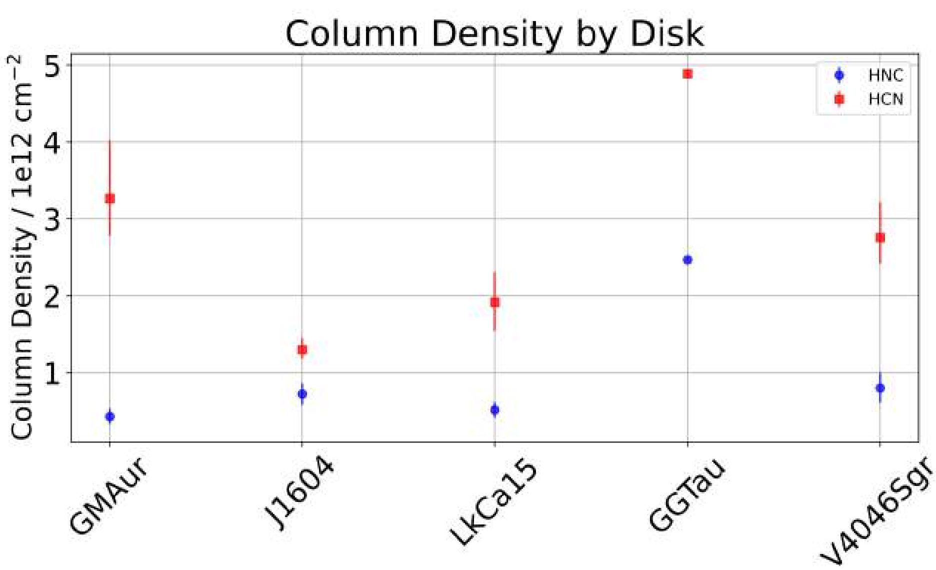

Figure 3. Column density of HNC (blue) and HCN (red) for each disk in the sample, as derived via rotational diagrams. We use the GG Tau column densities reported by Phuong et al. (2021). The uncertainties are shown as reported but are smaller than the marker.

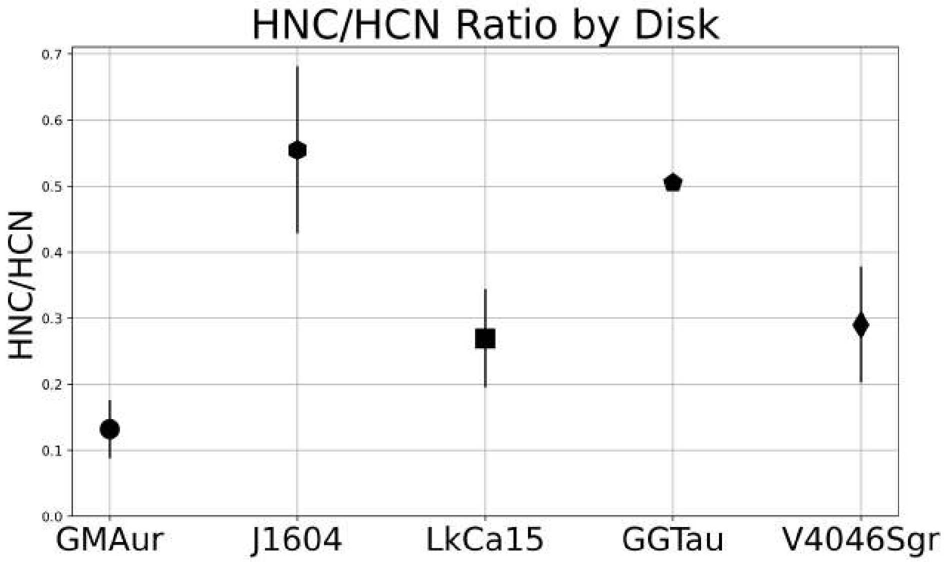

Figure 4. Ratio of HNC/HCN column densities for each disk in the sample, as derived via rotational diagrams. We use the GG Tau column densities reported by Phuong et al. (2021). The uncertainties are shown as reported but are smaller than the marker.

4. DISCUSSION

4.1. *New HNC Detections and Comparison to Prior Observations*

Our detections of the HNC J=3–2 emission line in V4046 Sgr, GM Aur, J1604, and LkCa 15 are each the first detections of HNC in those disks. This brings the total number of protoplanetary disks with HNC detected to 7, from three previously. Additionally, the detection of HNC J=4–3 in V4046 Sgr is the first detection of that line in PPDs. These transition disk detections, as well as the previous full-disk detections in TW Hya and HD 163296 (Graninger et al. 2015) and previous transition disk detection in GG Tau (Phuong et al. 2021) indicate that HNC may be a common molecule across protoplanetary disks. Although our sample size is small, the accessibility of the formation routes for HNC (Loison et al. 2014) suggests that HNC may as common as HCN. The magnitude of difference in fluxes between models and observations from the SMA, which has less sensitivity and spectral or angular resolution than ALMA, illustrates the importance of considering transition disks carefully. With these detections, each disk in our sample has HNC detected confidently (when including the Phuong et al. (2021) GG Tau results), despite using an interferometer besides ALMA. Furthermore, more sensitive facilities such as ALMA are likely able to confidently detect the HNC J=3–2 line as well as lines we were not consistently able to detect, including the J=1–0 and J=4–3 lines (although the J=2–1 line may not be observable due to water lines nearby). In fact, Long et al. (2021) mention a serendipitous HNC J=1–0 detection in transition disk J160830.7-382827 (Marel et al. 2018) for an ALMA survey of Lupus disks. Lee et al. (2024) additionally have detected HNC in a young star and its envelope. We are optimistic that as the number of large-sample surveys with interferometers increases, more HNC detections will be reported.

4.2. *Disk Chemical Modeling and Origins of HNC Chemistry*

Extensive modeling of the HCN and HNC chemical network in protoplanetary disks is explored in Long et al. (2021) for typical T Tauri and Herbig Ae stars, examining factors such as disk gas mass,

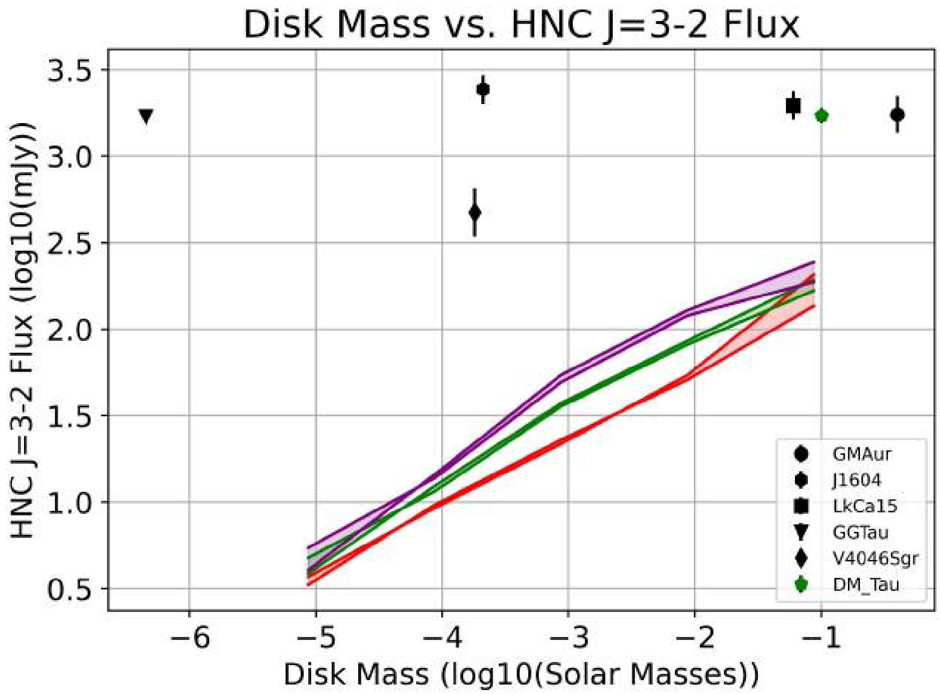

Figure 5. We show our measured HNC J=3–2 fluxes, in black (with GG Tau as an upper limit), as well as the LIME results for DM Tau (in green) (Long et al. 2024). These are compared to the modeling results from Long et al. (2021), and adjusted to a constant distance of 150 parsecs. Our transition disk fluxes are orders of magnitude stronger than the full-disk models predict, but the DM Tau model, which includes a millimeter-dust cavity, produces a flux in agreement with our data.

[C]/[H], [O]/[H], and [N]/[H] ratios, disk flaring, and UV radiation in full disks. These disks have no millimeter-dust cavity. Specifically they examine the two-dimensional spatial profile of each molecule as well as each molecule's intensity. Our measured disk-integrated fluxes for the HNC J=3–2 line are significantly higher (when normalized to a fixed distance of 150 pc to match the models) by an order of magnitude, as can be seen in Figure 5. As all of our sources are transition disks, we expect this discrepancy in fluxes to result from the lack of a cavity in their models.

To explore how transition disk HNC and HCN chemistry may differ, we use the published model of DM Tau described in Long et al. (2024). We extract HCN and HNC from these models and employ the Line Modeling Engine (Brinch & Hogerheijde 2010) to carry out the radiative transfer and excitation analysis. The code incorporates stellar mass, inclination, and systematic velocity of the disk as well as specific abundances of chemicals (Long et al. 2024). Using the same technique for measuring disk-integrated flux as described in Section 3.1, we find a flux of ≈1.7 Jy (when normalized to a distance of 150pc), significantly higher than the mean fluxes of ≈0.05 Jy from the Long et al. (2021) models and in agreement with our measurements from observations. Their model values for T Tauri stars are consistent with the results of HNC measurements (Graninger et al. 2015) in fellow T Tauri star TW Hya, a full disk, normalized to 150 parsecs. The discrepancy between the reported fluxes reinforces the importance of properly modeling spatial attributes of protoplanetary disks. As noted by Long et al. (2021), the UV flux in a transition disk is drastically altered from a full disk. They highlight that the permeation of UV flux through the outer disk will directly affect the produced HNC through its ion-based formation routes (Loison et al. 2014); they report that the outer disk's

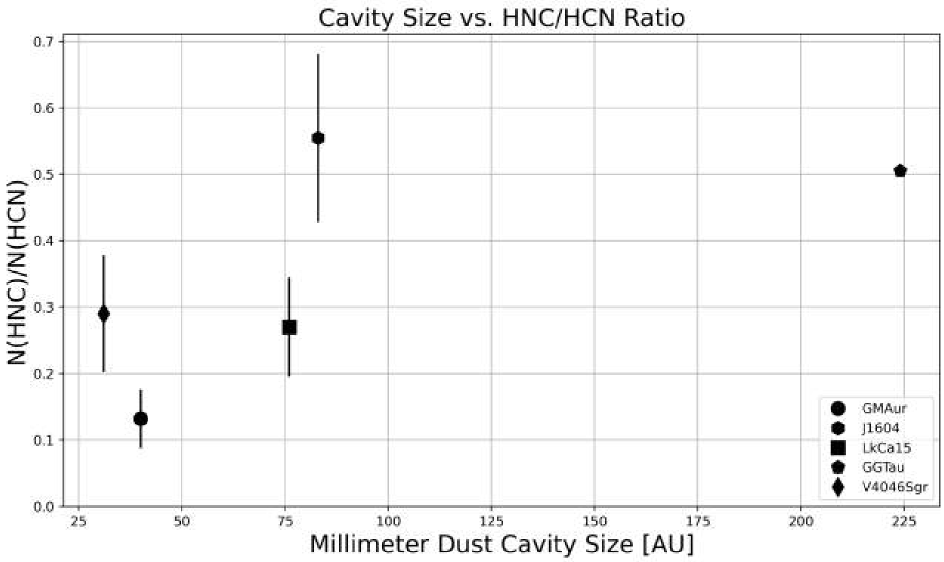

Figure 6. We show the HNC/HCN ratio for our sample compared to the cavity size of each disk. Most of our sample is clustered in a range of cavities smaller than 100 au. For GG Tau, the exception, we use the column densities reported by Phuong et al. (2021). The uncertainties are shown as reported but are smaller than the marker. There is no apparent trend between the points, indicating a lack of relationship between cavity size and HNC/HCN.

HNC/HCN ratio approaches unity in contrast to the inner disk's low HNC/HCN. We note concerns that if stellar radiation can penetrate deeper into the outer disk, the overall temperature of the region could be increased. In turn this could activate some of HNC's temperature-dependent destruction methods, such as reaction (3) as described in Table 1.

4.3. *HNC/HCN as a Tracer of Disk Properties*

With the column densities derived through the rotational diagrams, we can calculate the relative abundance HNC/HCN. The ratios for each disk are shown in Figure 4. Then we consider the variation in HNC/HCN with the size of the millimeter-dust cavity (as seen in Figure 6). The size of the cavity seems to have no coherent effect on amount of HNC compared to HCN. When compared to the discrepancy between our results and the Long et al. (2021) models, this may indicate that the presence of a substantial cavity, rather than the size of that cavity, has an effect on chemistry- perhaps in the distribution and movement of dust across the gap.

Literature (Long et al. (2021), Graninger et al. (2015)) predicts that this ratio approaches unity in the outer disk for full disks as the temperature-dependent destruction pathways become unavailable and ionizing UV flux becomes rare. To that end, within the limited context of our sample, we find that with increasing accretion rate, the HNC/HCN ratio decreases (Figure 7). To emphasize this point, we include on Figure 7 a point for TW Hya based on the HNC/HCN measurement from Graninger et al. (2015) and an estimation of accretion rate from Romanova et al. (2025). Although many other factors play a role in cyanide chemistry in protoplanetary disks, like carbon abundance, we surmise UV flux and permeation throughout the disk play major roles.

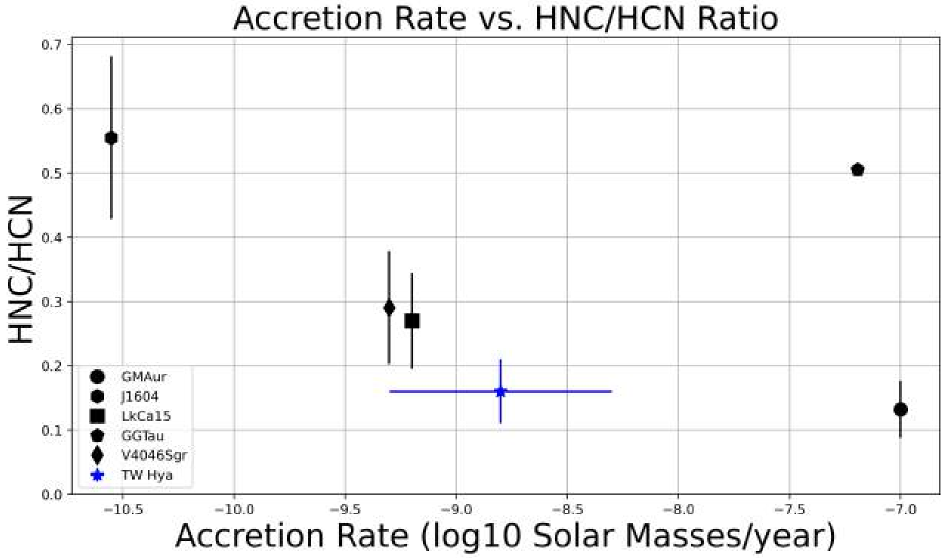

Figure 7. A scatterplot of stellar accretion rate for each disk versus the HNC/HCN column density ratio. There is a tentative downward trend with in HNC/HCN with increasing accretion. We include a point for TW Hya with an accretion rate from Romanova et al. (2025) and a HNC/HCN ratio from Graninger et al. (2015). Column densities for GG Tau obtained from Phuong et al. (2021), and uncertainties are smaller than the marker.

5. CONCLUSIONS

We present an analysis of multi-line HNC and HCN observations with the SMA in a sample of five transition disks. We conclude the following:

1. Using the Submillimeter Array, we find four new detections of the HNC J=3–2 emission line in transition disks around T Tauri stars, more than doubling the number of sources with HNC detected. We also place an upper limit on HNC in GG Tau.
2. We measure the disk-integrated HCN and HNC fluxes for the J=3–2 and J=4–3 emission lines and find them significantly higher than model predictions for full-disk HNC emission, which indicates the importance of the millimeter-dust cavity in chemical modeling.
3. We use a Markov chain Monte Carlo model to estimate rotational temperatures for HCN in each disk, and column densities for HCN and HNC in each HNC-detected disk, finding values around 10^{12} cm^{-2} and 10^{11} cm^{-2}, respectively.
4. We consider possible physical relationships between protoplanetary disk characteristics and ratios of column density, n(HNC)/n(HCN). Although we expect a relationship between the cavity size and the presence of HNC, we do not find one, and we suggest that the mere presence of a cavity alters HNC more dramatically than any particular size of that cavity. We do tentatively find an inverse relationship between accretion rate and HNC/HCN, implying that the UV radiation from the central star is a major factor in HNC chemistry.

We believe our measurements are enough to encourage further investigations of HNC as a potential radiation tracer in protoplanetary disks. All relationships discussed here are inherently tentative because of the small sample size but, with an increased sample size and perhaps a more sensitive instrument, a more compelling case can be built. We believe these results are motivating because of the relative insensitivity of the SMA when compared to top-of-the-line radio facilities like ALMA, and that transition disks have additional physical and chemical processes occurring that alter their environment when compared to a full disk. In all, HNC is an exciting new potential tracer of protoplanetary disk characteristics like accretion.

REFERENCES

Behrens, E., Mangum, J. G., Holdship, J., et al. 2022, The Astrophysical Journal, 939, 119, doi: 10.3847/1538-4357/ac91ce

Bergner, J. B., Öberg, K. I., Bergin, E. A., et al. 2019, The Astrophysical Journal, 876, 25, doi: 10.3847/1538-4357/ab141e

Brinch, C., & Hogerheijde, M. R. 2010, Astronomy & Astrophysics, 523, A25, doi: 10.1051/0004-6361/201015333

Carpenter, J. M., Ricci, L., & Isella, A. 2014, The Astrophysical Journal, 787, 42, doi: 10.1088/0004-637X/787/1/42

Condon, J. J., & Ransom, S. J. 2016, Essential radio astronomy, Princeton series in modern observational astronomy (Princeton: Princeton university press)

Donati, J.-F., Bouvier, J., Alencar, S. H., et al. 2019, Monthly Notices of the Royal Astronomical Society: Letters, 483, L1, doi: 10.1093/mnrasl/sly207

Dong, R., Marel, N. V. D., Hashimoto, J., et al. 2017, The Astrophysical Journal, 836, 201, doi: 10.3847/1538-4357/aa5abf

Endres, C. P., Schlemmer, S., Schilke, P., Stutzki, J., & Müller, H. S. P. 2016, Journal of Molecular Spectroscopy, 327, 95, doi: 10.1016/j.jms.2016.03.005

Espaillat, C., D'Alessio, P., Hernández, J., et al. 2010, ApJ, 717, 441, doi: 10.1088/0004-637X/717/1/441

Facchini, S., Benisty, M., Bae, J., et al. 2020, Astronomy & Astrophysics, 639, A121, doi: 10.1051/0004-6361/202038027

Flaherty, K., Hughes, A. M., Simon, J. B., et al. 2020, The Astrophysical Journal, 895, 109, doi: 10.3847/1538-4357/ab8cc5

Foreman-Mackey, D., Hogg, D. W., Lang, D., & Goodman, J. 2013, PASP, 125, 306, doi: 10.1086/670067

Gaia Collaboration, Vallenari, A., Brown, A. G. A., et al. 2023, A&A, 674, A1, doi: 10.1051/0004-6361/202243940

Goldsmith, P. F., & Langer, W. D. 1999, The Astrophysical Journal, 517, 209, doi: 10.1086/307195

Graninger, D., Öberg, K. I., Qi, C., & Kastner, J. 2015, The Astrophysical Journal, 807, L15, doi: 10.1088/2041-8205/807/1/L15

Guilloteau, S., Dutrey, A., & Simon, M. 1999, A&A, 348, 570

Hartigan, P., & Kenyon, S. J. 2003, ApJ, 583, 334, doi: 10.1086/345293

Hazelton, B. J., Jacobs, D. C., Pober, J. C., & Beardsley, A. P. 2017, The Journal of Open Source Software, 2, 140, doi: 10.21105/joss.00140

Huang, J., Andrews, S. M., Dullemond, C. P., et al. 2020, ApJ, 891, 48, doi: 10.3847/1538-4357/ab711e

Keppler, M., Penzlin, A., Benisty, M., et al. 2020, Astronomy & Astrophysics, 639, A62, doi: 10.1051/0004-6361/202038032

Kraus, A. L., & Hillenbrand, L. A. 2009, ApJ, 704, 531, doi: 10.1088/0004-637X/704/1/531

Law, C. J., Teague, R., Öberg, K. I., et al. 2023, ApJ, 948, 60, doi: 10.3847/1538-4357/acb3c4

Lee, S., Lee, J.-E., & Lee, S. 2024, Journal of Korean Astronomical Society, 57, 163, doi: 10.5303/JKAS.2024.57.2.163

Loison, J.-C., Wakelam, V., & Hickson, K. M. 2014, Monthly Notices of the Royal Astronomical Society, 443, 398, doi: 10.1093/mnras/stu1089

Long, D. E., Cleeves, L. I., Adams, F. C., et al. 2024, The Astrophysical Journal, 972, 88, doi: 10.3847/1538-4357/ad5c67

Long, F., Bosman, A. D., Cazzoletti, P., et al. 2021, Astronomy & Astrophysics, 647, A118, doi: 10.1051/0004-6361/202039336

Loomis, R. A., Cleeves, L. I., Öberg, K. I., et al. 2018, The Astrophysical Journal, 859, 131, doi: 10.3847/1538-4357/aac169

Macías, E., Espaillat, C. C., Ribas, Á., et al. 2018, ApJ, 865, 37, doi: 10.3847/1538-4357/aad811

Mamajek, E. E., & Bell, C. P. M. 2014, MNRAS, 445, 2169, doi: 10.1093/mnras/stu1894

Manara, C. F., Testi, L., Natta, A., et al. 2014, Astronomy & Astrophysics, 568, A18, doi: 10.1051/0004-6361/201323318

Marel, N. V. D., Williams, J. P., Ansdell, M., et al. 2018, The Astrophysical Journal, 854, 177, doi: 10.3847/1538-4357/aaaa6b

Martinez-Brunner, R., Casassus, S., Pérez, S., et al. 2022, MNRAS, 510, 1248, doi: 10.1093/mnras/stab3440

Müller, H. S. P., Schlöder, F., Stutzki, J., & Winnewisser, G. 2005, Journal of Molecular Structure, 742, 215, doi: 10.1016/j.molstruc.2005.01.027

Müller, H. S. P., Thorwirth, S., Roth, D. A., & Winnewisser, G. 2001, A&A, 370, L49, doi: 10.1051/0004-6361:20010367

Owen, J. E., Ercolano, B., & Clarke, C. J. 2017, Monthly Notices of the Royal Astronomical Society, 472, 2955, doi: 10.1093/mnras/stx2261

Phuong, N. T., Dutrey, A., Di Folco, E., et al. 2020, A&A, 635, L9, doi: 10.1051/0004-6361/202037682

Phuong, N. T., Dutrey, A., Chapillon, E., et al. 2021, Astronomy & Astrophysics, 653, L5, doi: 10.1051/0004-6361/202141881

Phuong, N. T., Dutrey, A., Chapillon, E., et al. 2021, A&A, 653, L5, doi: 10.1051/0004-6361/202141881

Preibisch, T., & Feigelson, E. D. 2005, ApJS, 160, 390, doi: 10.1086/432094

Quast, G. R., Torres, C. A. O., de La Reza, R., da Silva, L., & Mayor, M. 2000, IAU Symposium, 200, 28

Romanova, M. M., Espaillat, C. C., Wendeborn, J., et al. 2025, Monthly Notices of the Royal Astronomical Society, 538, 480, doi: 10.1093/mnras/staf148

Rosenfeld, K. A., Andrews, S. M., Wilner, D. J., & Stempels, H. C. 2012, The Astrophysical Journal, 759, 119, doi: 10.1088/0004-637X/759/2/119

Stadler, J., Benisty, M., Izquierdo, A., et al. 2023, A&A, 670, L1, doi: 10.1051/0004-6361/202245381

Teague, R. 2019, The Journal of Open Source Software, 4, 1632, doi: 10.21105/joss.01632

Teague, R. 2019, The Journal of Open Source Software, 4, 1632, doi: 10.21105/joss.01632

—. 2020, richteague/keplerian_mask: Initial Release, 1.0, Zenodo, doi: 10.5281/zenodo.4321137

Teague, R., Bae, J., Aikawa, Y., et al. 2021, ApJS, 257, 18, doi: 10.3847/1538-4365/ac1438

Van Der Marel, N. 2023, The European Physical Journal Plus, 138, 225, doi: 10.1140/epjp/s13360-022-03628-0

Visser, R., Bruderer, S., Cazzoletti, P., et al. 2018, Astronomy & Astrophysics, 615, A75, doi: 10.1051/0004-6361/201731898

Williams, J. P., & Cieza, L. A. 2011, Annual Review of Astronomy and Astrophysics, 49, 67, doi: 10.1146/annurev-astro-081710-102548

Öberg, K. I., Facchini, S., & Anderson, D. E. 2023, Annual Review of Astronomy and Astrophysics, 61, 287, doi: 10.1146/annurev-astro-022823-040820